Catalysis Today 419 (2023) 114134

Contents lists available at ScienceDirect

Catalysis Today

journal homepage: www.elsevier.com/locate/cattod

Titania nanorods array homojunction with sub-stoichiometric TiO_2 for enhanced methylene blue photodegradation

Nicolò Spigariol [a,1], Letizia Liccardo [a,1], Edlind Lushaj [a], Enrique Rodríguez-Castellón [b], Isabel Barroso Martin [b], Federico Polo [a], Alberto Vomiero [a,c,*], Elti Cattaruzza [a], Elisa Moretti [a,**]

[a] Department of Molecular Sciences and Nanosystems, Ca' Foscari University of Venice, Via Torino 155, 30172 Venezia, Mestre, Italy
[b] Department of Inorganic Chemistry, Cristallography and Mineralogy (Unidad Asociada al ICP_CSIC), Faculty of Sciences, University of Malaga, Campus de teatinos, 29071 Malaga, Spain
[c] Division of Materials Science, Department of Engineering Sciences and Mathematics, Luleå University of Technology, 97187 Luleå, Sweden

ARTICLE INFO

Keywords:
Photocatalysis
TiO_2/TiO_{2-x}-scheme homojunction
Nanorods
Wastewater treatment

ABSTRACT

TiO_2 thin films are known to promote photodegradation of dyes and pollutants in water solution via heterogeneous photocatalysis. This ability is guided by the photoexcitation through photons having energies above the band gap. To improve photocatalytic activity, nanostructures with high surface area can be applied, which can ease molecular adsorption/desorption mechanisms, enhance electronic transfer properties and lower excitation energy. For this purpose, square cross-section TiO_2 vertically aligned nanorod (TNR) array configuration has been chosen as a semiconductor substrate. On top of it, a thin layer of sub-stoichiometric TiO_{2-x} has been deposited, aiming at inducing a vacancy doped homojunction between two different oxygen rich/deficient TiO_2 layers, possibly leading to lower band gap and enhanced photochemical activity. In principle, promotion of electron and holes separation and suppression of charge recombination could occur. Vertically aligned TNRs have been deposited through a hydrothermal growth in acidic conditions on a pre-seeded glass conducting substrate, optimizing the seeding process through spin coating. Sub-stoichiometric TiO_{2-x} layer (50 nm nominal thickness) has been deposited on top of TNRs via radiofrequency magnetron sputtering at three different stoichiometries, tuning the oxygen partial pressure in sputtering argon atmosphere at 10 %, 15 % and 20 %, respectively. Photocatalytic activity has been investigated in the photodegradation of an aqueous solution of methylene blue, both under UV and simulated solar light irradiation at room temperature and atmospheric pressure, resulting in the degradation of methylene blue target molecule up to 99 % under UV and 85 % under simulated solar irradiation after 6 h. These promising achievements unlock new environmental applications for enhanced dye degradation industrial processes.

1. Introduction

Nowadays, the introduction and spread of numerous pollutants in water sources coming from industrial manufacturing processes made water contamination one of the most pressing issues. Textile industry, among others, is one of the major responsible for releasing a large quantity of dyes coming from the incomplete fixation of fabrics able to resist to oxidizing and reducing agents [1–3]. According to the US EPA (United States Environmental Protection Agency), during a typical dyeing process about 40 L of clean water are required per kilogram of fabrics. Consequently, ecosystems and human health are negatively affected [4,5], especially if such wastewaters are directly discharged without a suitable treatment process. In this regard, photocatalytic advanced oxidation processes (AOPs) have been gaining attention to accelerate oxidation and degradation of a wide range of organic pollutants in wastewater [6]. As predicted by G. Ciamician in his visionary article in 1912 [7], photochemistry is now becoming a popular topic because it is considered a sustainable way to perform chemical reactions and degrade pollutants exploiting solar energy. Combining this strategy with the ability of semiconductor materials to interact with a suitable

* Corresponding author at: Department of Molecular Sciences and Nanosystems, Ca' Foscari University of Venice, Via Torino 155, 30172 Venezia, Mestre, Italy.
** Corresponding author.
E-mail addresses: alberto.vomiero@ltu.se (A. Vomiero), elisa.moretti@unive.it (E. Moretti).
[1] These authors contributed equally to this work.

https://doi.org/10.1016/j.cattod.2023.114134
Received 19 December 2022; Received in revised form 20 March 2023; Accepted 24 March 2023
Available online 25 March 2023

wavelength, electron-hole pairs able to degrade molecules via a radical mechanism are produced [8,9]. Many semiconductors have been investigated and tested as promising photocatalysts but, among them, titania (TiO_2) is still the most widely used [10]. In fact, this material shows excellent chemical properties, being at the same time cheap, non-toxic, and stable. Furthermore, thanks to its ease of synthesis, it is possible to tune crystallinity, polymorph composition, morphology, surface area and particle size. There are several chemical and physical methods that can be exploited to synthesize TiO_2 nanoparticles (NPs) in the form of powders or thin films. Physical vapor deposition (PVD) methods, such as radiofrequency (RF) magnetron sputtering, are widely used to obtain thin films with controlled thickness, desired composition, high purity, and strong adhesion to the substrate [11,12]. The use of thin films, instead of powders, displays many advantages, among which the possibility to synthesize these films on a substrate, making them easily recoverable. Additionally, combining different morphologies appears to be one of the most appealing strategies to increase the overall performances of the photocatalyst [13]. In fact, the higher the surface area, the higher the possibility to have an increased number of active sites at the surface. Rutile nanorods (NRs) grown on the surface of a fluorine-doped tin oxide glass (FTO) have been extensively studied and recently considered effective in the field of heterogeneous catalysis. A possible strategy to easily recover the catalyst from the system after the treatment process involves the combination of the large surface area of the rod-like shape with the non-dispersed bulk feature. Moreover, NRs configuration can be suitable for the photodegradation of organic pollutants under UV light. In this regard, several studies have been reported in literature, stating the effectiveness of rod configuration especially for the delay on the charge carriers' recombination and the availability of active sites exposed at the surface. In detail, the delaying on the charge-carriers recombination may be ascribed to quantum confinement due to size effect (nanorods radius smaller than the exciton Bohr radius), as well as surface and bulk trapping effect [14,15]. However, if not properly designed, pure TNRs may have several drawbacks, such as wide band gap (from 3.0 eV of rutile up to 3.2 eV of anatase) and high rate of charge recombination. To improve the overall photocatalytic performances of this material, different strategies have been proposed. Several authors reported that a vacancy doped homojunction induced in the TiO_2 array could efficiently enhance the properties of UV-Visible driven photocatalytic processes of the material [16,17]. Based on these considerations, the controlled introduction of a thin film of sub-stoichiometric TiO_{2-x} over the surface of TiO_2 NR array may be an interesting approach to influence the oxygen vacancies parameter. TiO_{2-x} thin layer can be easily created by a RF sputtering deposition by inducing a larger deficiency of oxygen (lowering the partial pressure of oxygen in the working gas), leading to the formation of a homojunction between the NR structure and the sub-stoichiometric TiO_{2-x}. Therefore, the combination of pure and sub-stoichiometric titania may lead to several advantages: the composite system could show changes in its electronic structure, broadening its absorbance ability, and enhancing its photocatalytic properties compared to the bare material. For instance, the vacancy doped TiO_{2-x} surface layer is reported to interact with the TiO_2 NR promoting the separation between electrons and holes simultaneously suppressing recombination [17,18]. Furthermore, TiO_{2-x} shows a narrower band gap in comparison to stoichiometric titanium dioxide, typically about 1.5 eV, and tunable according to the synthetic method, thus leading to an increase in the visible light absorption [19,20]. In this work, the role of TiO_{2-x} titania thin films deposited via RF magnetron sputtering was investigated, comparing the photocatalytic performances of pure and sputtered TiO_2 NR samples. Homojunctions were prepared tuning two parameters: the number of cycles for the creation of the seed layer to induce the growth of TNRs and the O_2 partial pressure of the vacuum chamber during sputtering deposition. The films were tested in a photodegradation reaction in water solution under UV and solar light irradiation at room temperature (RT) and P atm, taking methylene blue (MB) as a dye probe, correlating the photocatalytic activity and the physicochemical and optical properties of the samples.

2. Experimental

2.1. Materials

Titanium (IV) butoxide (TBOT), absolute ethanol (EtOH), acetic acid (HAac), hydrochloric acid (37 % v/v), sodium hydroxide and methylene blue (MB) were all analytical grade and purchased by Sigma Aldrich without further purification. Fluorine tin oxide (FTO) glasses were purchased by Pilkington.

2.2. FTO substrates preparation

FTO glasses were ultrasonically cleaned for 5 min three times, each in a different solvent: absolute ethanol, deionized water, and acetone, respectively. Cleaned samples were then dried in a stream of nitrogen and then stored at room temperature.

2.3. TiO_2 nanorods synthesis

Titania Nanorods (TNR) were synthesized through hydrothermal growth method. Two different solutions, a seed layer solution (A) and a NR growth solution (B), were used during the process. Solution A was prepared mixing 10^{-3} mol of titanium(IV) butoxide in a solution of absolute ethanol and acetic acid in molar ratio 1:5 under stirring for 2 h before being left aging 24 h at RT. Seed solution was then deposited on the conductive side of a FTO glass by spin coating at the rate of 500 rpm for 5 s and 3000 rpm for 30 s. The FTO glass was then heated at 120 °C for 10 min in air flow. Samples were labelled as single layer (SL) and double layer (DL) when this procedure had been repeated one or two times respectively. Finally, the samples were annealed in a furnace at 450 °C for 1 h in air flow. Solution B, containing titanium butoxide 0.03 M, was prepared by adding $1.2 \bullet 10^{-3}$ mol of titanium butoxide to a solution of hydrochloric acid and deionized water (1:1 v/v). The as obtained solution B was stirred for 5 min until the solution was colorless transparent. The FTO substrates were placed on a Teflon support inside a Teflon-line of a stainless-steel autoclave (40 mL). Solution B was transferred in the Teflon-line and the hydrothermal growth was carried out at 150 °C for 4 h. Lastly, the samples were washed with deionized water and dried at 60 °C for 2 h.

2.4. TiO_2 thin films deposition

The desired TiO_2/TiO_{2-x} homojunctions were obtained by physical vapor deposition (PVD). TiO_{2-x} nanostructures were synthesized by reactive sputtering deposition on TiO_2 NR (TNR) surface in a custom-made RF (radiofrequency) magnetron sputtering deposition apparatus. Depositions were performed starting from a target of pure metallic titanium by using a 13.56 MHz RF source and three reactive atmospheres $Ar+O_2$: 90 % + 10 %, 85 % + 15 % and 80 % + 20 %. The total pressure was $50 \bullet 10^{-4}$ mbar in dynamic vacuum conditions and the sample holder was rotated at 5 rpm during deposition to improve homogeneity of the film composition and thickness. The RF power to the 2 in. diameter titanium target was fixed at 250 W. During the deposition, temperature was lower than 60 °C to avoid induced phase transition. The deposition duration was around 1 h according to the desired film thickness of titanium between 50 and 60 nm (as obtained by a stylus profilometer, with relative uncertainty around 20 %), depending on the reactive atmosphere used. Samples were referred to as: XTNRY, where X stands for SL or DL and Y for 10 %, 15 %, 20 % of O_2 in Ar. For instance, sample SLTNR10 is made using a single layer of seed solution and it has been sputtered under a 10 % O_2 in Ar atmosphere (See Table 1).

Table 1
Sample label, layer type, working gas composition and deposition time of the synthesized photocatalysts.

Sample label	Seed layer type	Working composition ($Ar + O_2$, %)[a]	Gas deposition time (s)
SLTNR	Single	-	-
DLTNR	Double	-	-
SLTNR10	Single	90 + 10	3600
DLTNR10	Double	90 + 10	3600
SLTNR15	Single	85 + 15	4000
DLTNR15	Double	85 + 15	4000
SLTNR20	Single	80 + 20	4685
DLTNR20	Double	80 + 20	4685

[a] Total pressure = $50 \bullet 10^{-4}$ mbar.

2.5. Characterization

The morphology of bare and sputtered TNR was characterized using a field-emission scanning electron microscope (FEG-SEM, Zeiss Sigma 174 Cz). Morphology was further characterized using a Bruker Dimension ICON AFM in tapping operation mode with a Bruker SCM-PIT-V2 probe having a Platinum-Iridium coated electrically conductive tip (spring constant ~ 0.3 N/m, nominal tip radius ~ 25 nm). Crystal structure was examined by X-ray diffraction (XRD) using an X-ray diffractometer (Philips PW1050/37) with Cu K_α radiation ($\lambda = 1.5418$ Å). Diffuse reflectance UV-Visible absorption spectra (DRUV-Vis) were investigated to compare the light-harvesting ability of bare and modified samples. The DRUV-Vis spectra of the samples were collected with a Cary100 UV-Vis spectrophotometer using and integrating sphere accessory and $BaSO_4$ as a reflectance standard during the measurements. The surface of the materials was studied by X-ray photoelectron spectroscopy (XPS). The high-resolution C 1s, O 1s, Ti 2p and N 1s core level spectra were registered using a Physical Electronics PHI 5700 spectrometer with non-monochromatic Al-K_α radiation (1486.6 eV), recorded in the constant pass energy mode at 29.35 eV with a 720 μm diameter analysis area. Adventitious carbon (C 1s at 284.8 eV) was used as a reference. We are well aware that this signal usually falls in a very large binding energy range (284.0–285.6 eV, as reported in literature), thus making difficult a consistent energy calibration of the binding energy scale [21,22]; however, the present choice gives for our samples reliable BE values for all the detected XPS bands. A Shirley-type background was subtracted from the signals and the deconvolution curves were fitted using Gaussian–Lorentzian model in Multipak 9.0 software. The materials were also studied after etching with Ar^+ at 1 keV for 1 min.

2.6. Photocatalytic degradation experiments

To evaluate the photocatalytic activity of the synthesized materials under both UV and visible light irradiation, MB degradation was selected as a test reaction. All the photocatalytic tests were carried out in a glass reactor containing 50 mL of 6×10^{-6} M MB aqueous solution with constant stirring at 30 °C and placing the glass samples on a Teflon support. The solution containing the photocatalyst was kept in dark for 30 min to reach MB adsorption/desorption equilibrium. The photocatalytic tests under UV light were carried out using a 125 W high pressure mercury lamp, operating at wavelengths between 180 and 420 nm with a peak at 366 nm and the sputtered glass samples were placed right underneath the lamp's filament at a distance from the glass surface of 10 cm. To explore the possibility of solar-driven photocatalysis a solar simulation has been performed using a M-LS Rev B solar simulator from ABET technologies with a 100 Watts xenon lamp. Standard cell is set to measure a 130 mA current when exposed to 1 Sun of solar irradiance. Calibration revealed the required distance to be around 12.5 cm between the sample surface and the light source. Afterward, the glasses were exposed to the light irradiation under ambient conditions and aliquots of 0.7 mL of the aqueous solution were collected from the reactor at fixed intervals up to 6 h. A Cary100 UV-Vis spectrometer was used for the determination of the MB concentration, after calibration. The degradation processes were monitored following the absorbance at the maximum of the UV-Vis spectrum of the target molecule (664 nm). Since its photodegradation pathway is well known, the possible formation of byproducts was monitored acquiring the overall UV–Vis spectrum of the solutions recovered at different times during the degradation experiments [23].

The rate constant was calculated according to the following Eq. (1):

$$\ln \frac{C}{C_0} = -kt \quad (1)$$

where C is the concentration after time t, C_0 represents the initial concentration and k is the pseudo-first order rate constant (min^{-1}), calculated as (2):

$$k = 2.303 \times slope \quad (2)$$

To evaluate the stability and reusability of the photocatalysts, a 3-cycle recycling test was performed. The sample was washed with deionized water and dried overnight after each photocatalytic cycle for the recycling test. To explore the effect of surface activity in acidic or basic conditions two photocatalytic tests were carried out by adjusting the pH at 4.0 and 9.0 both with sample SLTNR20.

3. Results and discussion

3.1. Structural and morphological characterization

According to single or double seed-layer (SL or DL) deposition, two different series of samples were produced with three different sputtering atmospheres: 10 %, 15 % and 20 % oxygen in argon, respectively (See Table 1, Section 2).

In Fig. 1(a–d), SEM images of the samples are reported showing the morphology of the TNRs before and after the sputtering deposition. In Figs. 1a and 1b it can be noticed the presence of nanostructured vertically aligned TNRs for both the SL and DL, which are closely packed and uniformly covering the surface of the FTO, proving the effectiveness of the seed layer procedure. It must be pointed out that a not uniform seed deposition can create the so-called dried-soil pattern, which leads to the presence of voids and cracks on the array. All rods appeared with a square cross section geometry with a rather uniform average size. Two different calculation methods were applied to better estimate the average size: software analysis and intercept method [24] (see Supplementary material). The latter method is typically applied to determine the grain size dimension in alloys and polycrystalline materials. However, since TNR are not perfectly packed but very close together, this approach is supposed to give a reasonable rough estimate for the average diameter. The results are shown in Tables S1 and S2. Values of (78 ± 4) nm for SL and (68 ± 5) nm for DL can be compared with SEM micrographs measurements confirming the intercept method is a suitable alternative to software imaging. Thanks to the cross-section imaging analysis, the average TNR layer thickness was estimated around 310 ± 63 nm for SLTNR and 350 ± 84 nm for DLTNR. Fig. 1c–d shows the SEM images of the post sputtered samples, revealing the presence of newly grown nanorods on the pristine TNR surface. The as-obtained TiO_{2-x} rods are thinner and they homogeneously cover the NR surface, thus indicating the effectiveness of the sputtering deposition procedure.

In addition to SEM, AFM topography images of SLTNR and SLTNR15 nanorod arrays (Figs. 2a and 2b, respectively) acquired in tapping mode show an overall uniform coverage. Moreover, it can be observed the presence of much thinner nanorods in the sputtered sample, suggesting a second growth onto the pre-existing nanostructures. These observations are in good agreement with the SEM measurements (Figs. 1c and 1d).

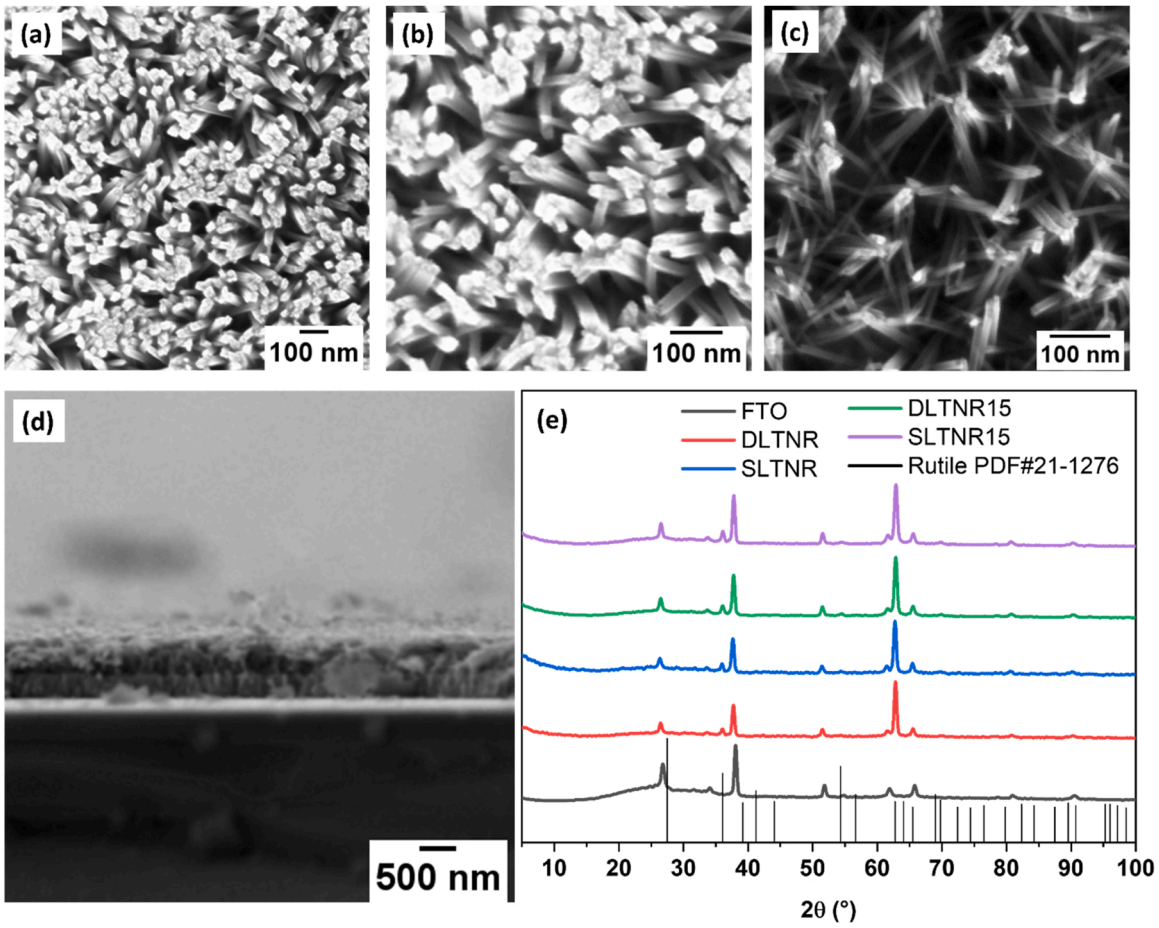

Fig. 1. (a–d) SEM images of bare (a) SLTNR and (b) DLTNR at different magnifications and after the sputtering deposition (d) from top and (e) cross-section view (e) XRD diffractogram comparing pristine FTO glass and both stages of seed (SLTNR, DLTNR) and sputtered layers (SLTNR15 and DLTNR15).

This was further confirmed by the line profiles of the SLTNR and SLTNR15 (Supplementary material, Fig. S3a and S3b) that allowed to estimate the lateral size of the nanostructures. Nanorods with a lateral dimension ranging from about 75–87 nm were detected in the SLTNR sample, while the sputtered sample (SLTNR15) showed a more uniform surface, presenting features with a smaller diameter (about 17–25 nm).

Moreover, the surface roughness parameter of a material highlights the differences depending on the irregularity of the profiles. For vertical profiles such as the nanorods reported in this study, the surface roughness is evaluated from amplitude parameters, among which the root mean square (rms) roughness (Rq) is included. Rq is a measure of the standard deviation of the Z height [25] and its extrapolated value for SLTNR and SLTNR15 was 19.6 nm and 2.2 nm, respectively. A higher value of Rq for SLTNR can be explained by the fact that the nanostructures are not perfectly packed, as previously observed from SEM analyses (Fig. 1). The decrease in roughness highlighted by AFM results indicates that the introduction of sub-stoichiometric TiO_{2-x} induces a secondary growth of much thinner nanorods on top of the starting TiO_2 nanostructures.

Fig. 1e shows the XRD patterns for all the samples of TNR grown on FTO glasses before and after the sputtering process. SLTNR and DLTNR samples show a peak at 2θ of 36° identified with (101) peak of rutile crystalline phase of TiO_2 nanorods and 2θ of 64° identified as the (002) peak accounting for the vertically aligned structure of the rods growing perpendicularly to the surface of the FTO along the [001] direction [26]. Consequently, it can be affirmed that for all the samples there is a clear preferential orientation of the rutile phase, which calls for a single crystal growth perpendicular to the FTO substrate. It should be considered that several factors are playing a crucial role in the TNR growth, one in particular is the amount of the titanium precursor in the seed and hydrothermal growth solution. Rutile nanorods crystallinity is enhanced as the quantity of titanium butoxide is increased. Samples SLTNR15 and DLTNR10 contained 10 % more titanium precursor than the other samples.

3.2. XPS analysis

The surface chemical composition of the materials (in atomic concentration %) is shown in Table 2. This table also includes the composition after etching 1 min with Ar^+. The studied materials present a high concentration of carbon that is almost totally removed after etching. Samples DLTNR20 and SLTNR20 also present Si.

All the samples exhibit a high content of carbon on the surface. The high-resolution C 1*s* core level spectra (Fig. 3-left panel and Table 2) show different functional groups on the surface. All the spectra can be decomposed in four contributions at about 284.8, 286.2, 287.5 and 288.7 eV. The main contribution at 284.8 eV comes from the presence of -C—C- and -C═C- bonds mainly from adventitious carbon. The second contribution at 286.1–286.3 eV is assigned to C—O and C—N bonds. The third and fourth contributions are very weak and appear at 287.5–287.6 eV and 288.7–288.8 eV and are assigned to residual C═O and carboxylate groups, respectively [27,28]. The relative intensities of these contributions are slightly modified with the different treatments. Upon Ar^+ etching, the surface content of carbon is dramatically reduced, indicating that most of the surface carbon comes from adventitious contamination.

O 1*s* core level spectra (not reported) can be decomposed in three contributions. The main contribution at 529.8–529.9 eV is assigned to

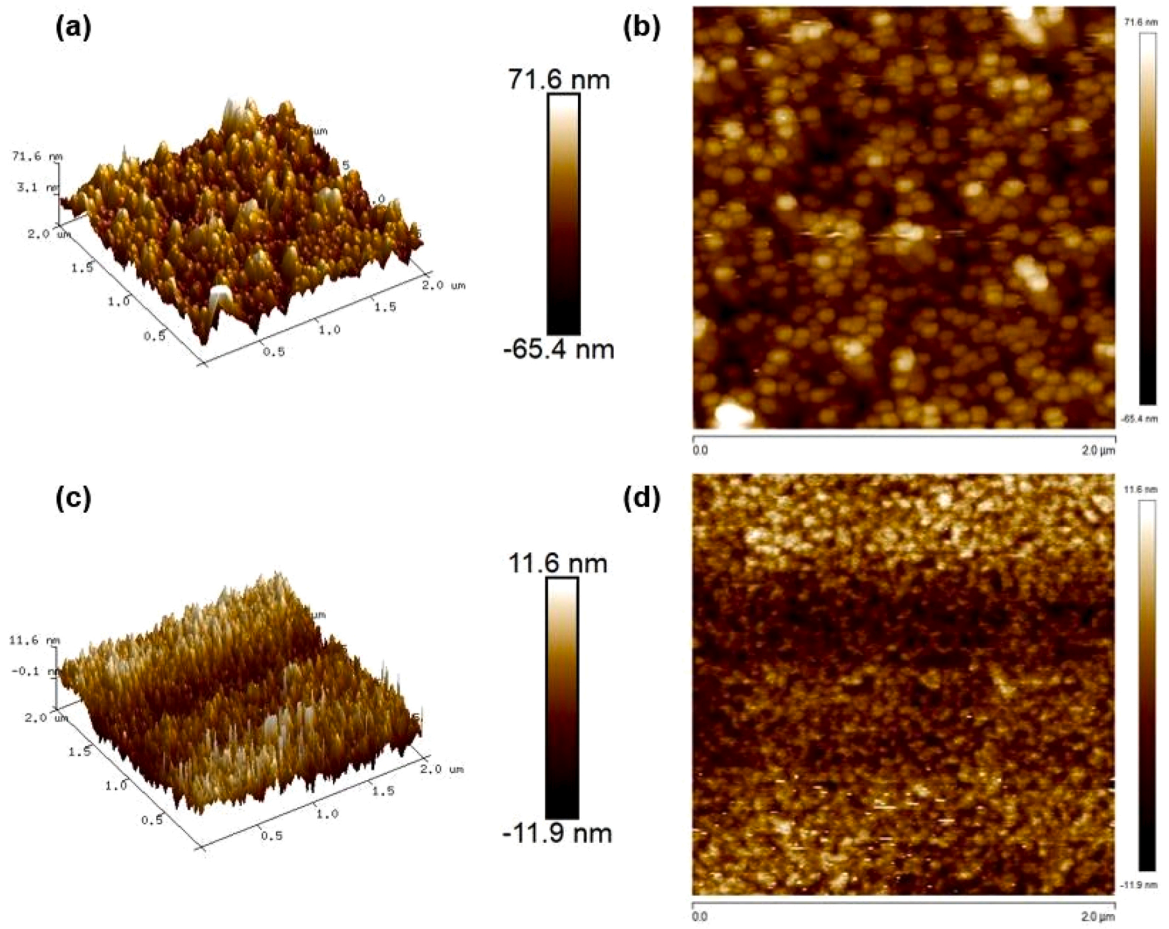

Fig. 2. AFM 3D morphologies of (a) SLTNR and (c) SLTNR15 samples. AFM 2D images of (b) SLTNR and (d) SLTNR15 nanorod arrays.

Table 2
Surface chemical composition (in atomic concentration %) determined by XPS.

Sample	C	O	N	Ti	Si
DLTNR10	44.7	42.0	-	13.3	-
SLTNR10	48.3	37.6	2.5	11.6	-
DLTNR15	44.8	40.3	1.3	13.6	-
DLTNR20	45.1	38.2	1.2	11.5	4.0
SLTNR20	47.3	36.9	1.6	9.9	4.3
DLTNR10[a]	10.9	61.7	-	27.4	-
SLTNR10[a]	12.3	60.1	1.0	26.6	-
DLTNR15[a]	11.2	60.7	0.8	27.3	-
DLTNR20[a]	9.2	61.6	0.8	30.0	1.4
SLTNR20[a]	10.5	59.4	1.1	26.9	2.1

[a] After etching 1 min Ar*.

lattice oxygen of titania [29]. The second contribution at 531.5–531.8 eV is assigned to surface oxygen mainly as Ti-OH groups and carboxylate. The relative intensity of this contribution is higher for SL samples than for DL samples. The third contribution at higher binding energy is assigned to C-O bonds and water.

The high-resolution Ti 2*p* core level spectra in the different samples (Fig. 3 – central panel) are very similar, with Ti $2p_{3/2}$ binding energies falling at 458.4–458.6 eV, typical of titania [29]. The Ti $2p_{3/2}$ signal is always symmetric and Ti(IV) species are the main ones. However, after a mild etching with Ar^+ plasma, the presence of sub-stoichiometric titania is observed too, as shown by the lower BE 2*p* doublet overlapping the Ti (IV) signals (Fig. 3-right panel).

In the five samples, the mean distance between these two different 2*p* signals is around 1.5 eV. We suppose that the first few nm of our sub-stoichiometric titania coatings completely oxidized as a consequence of the interaction with the environmental oxygen. The mild sputtering needed for removing the surface contamination allowed to detect the as-deposited sub-stoichiometric titania. Considering a rough comparison between the intensity of the two different Ti 2*p* signals, the sub-stoichiometric titania should have a O/Ti ratio ranging between 1.8 and 1.9.

An explanation of the presence of nitrogen in some samples may be ascribed to contamination induced by an incorrect handling of the sample. Upon Ar^+ etching the nitrogen content decreases, confirming its presence at the sample surface only.

Samples DLTNR20 and SLTNR20 show the presence of Si, probably coming from the leaching of the glass substrate under hydrothermal conditions. Aforementioned Si is present as Si(IV) and the oxygen combined with Si appears as a part of the contribution at high binding energy in the O 1*s* core level spectra. No traces of F and Sn from FTO were detected on the surface of all studied materials.

3.3. Optical studies

To investigate the optical properties of the prepared junctions, the Uv-Vis absorption spectra were recorded, and the results are shown in Fig. 4. TNR sample is showing the typical TiO_2 strong absorption in the UV region with a band-edge slightly shifted toward the visible region with respect to the pristine FTO glass absorption. Thanks to the homo-junction formation, the absorption edge is showing a considerable redshift with an extension of the overall absorption toward higher wavelengths up to ∽ 800 nm. It is worth noting that samples appeared red-shifted with decreasing concentration of oxygen in deposition

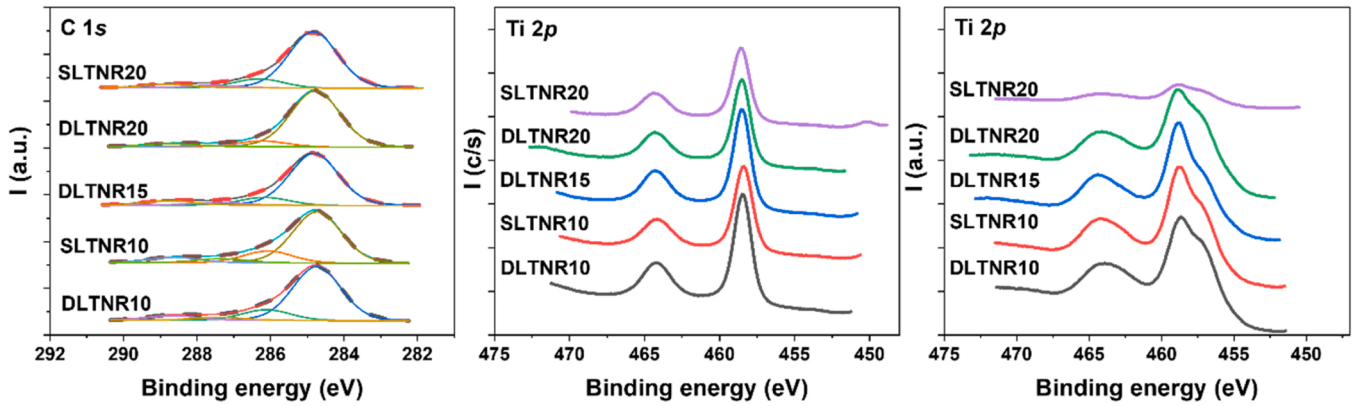

Fig. 3. High resolution XPS bands: C 1s (on the left), Ti 2p before (on the center) and after (on the right) mild Ar^{+} sputtering for removing surface contamination.

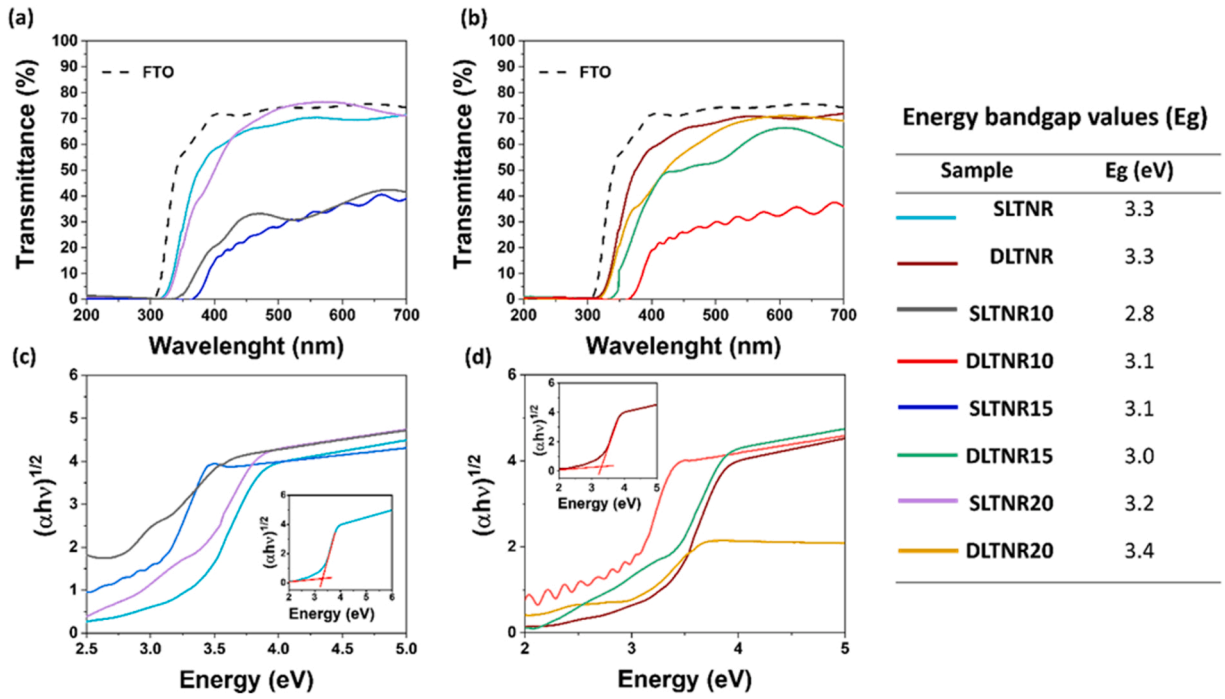

Fig. 4. : Transmittance UV-Vis spectra (top) and Tauc plots (bottom) referring to (a, c) SLTNRX series and (b, d) DLTNRX series. The energy band gap values are listed in the inset table.

working-gas (from 30 % to 10 %), hence with titanium dioxide being more sub-stoichiometric, as expected. Oscillations above 400 nm may be associated with interference effects rising from internal reflections. The improved spectral response can be attributed to the homojunction formation between TiO_2 and TiO_{2-x} [16]. To better understand the junction mechanism, the band gap of the samples was extrapolated from Tauc plots using the baseline approach method for indirect band gap (Fig. 4) [30]. The band gap energies are presented in the Fig. 4. As it can be noticed, band gap energies exhibit a direct correlation with increasing stoichiometry in deposited layer TiO_{2-x} composition: the lowest value is measured in SLTNR10 sputtered sample (2.8 eV), while the highest is measured in SLTNR20 (3.4 eV). In addition to the redshift of the absorption onset, optical spectra showed an increased absorption in the full visible spectral range after the deposition of the sputtered layer. As expected, the absorption is stronger in samples with larger oxygen sub-stoichiometry, as clearly visible in Fig. 4. This suggests a potential enhancement in the catalytic properties towards the photo-degradation of MB under simulated solar illumination.

3.4. *Photocatalytic activity*

Methylene Blue (MB), a heterocyclic aromatic compound and a well-known pollutant dye, was taken as the photocatalytic probe molecule. MB photodegradation pathway is well known and deeply investigated through liquid chromatography-mass spectroscopy and gas chromatography-mass spectroscopy analyses, under UV light and in the presence of TiO_2 based materials. It is based on the conversion of the organic dye into harmless compounds such as CO_2, nitrate, ammonium, and sulphate ions [23]. During the photocatalytic tests, the absorbance values have been measured following the 664 nm peak evolution, which is the maximum value of MB typical absorption band. To test the photo activity of the sputtered samples, they were tested under both UV and simulated solar light irradiation, and UV-Visible spectra were recorded and monitored in the range 300–800 nm at different photoreaction times (after 5, 10, 20, 40, 60, 90, 120, 180, 240, 300 and 360 min), also investigating the possible presence of Leuco Methylene Blue (LMB) in solution. LMB is a colorless reduced form of MB, which can be produced during the experiment and can be rapidly reduced back to MB. It is stable

in a vacuum or under inert atmosphere and as the MB, it exhibits a characteristic and strong absorbance band at 520 nm [31]. Fig. 5a and b show the MB UV-Vis absorption spectra in dark mode and under both UV light and solar simulated irradiation for the samples SLTNR15 and DLTNR15, taken as examples. The decrease in the absorption at 664 nm can be ascribed to the degradation of benzene rings and heteropoly aromatic linkages. The LMB typical band was not detected, hence the reduced colorless form of MB was not present in the reaction environment neither under UV nor under simulated solar light and the sample solution bleaching was exclusively due to the MB degradation.

In Fig. 5c-f the photocatalytic performances of the NRs series are presented under both UV and simulated solar light irradiation. While the corresponding degradation efficiencies, the pseudo-first order kinetic constant values and uncertainty $k \pm \delta_k$ (10^{-3} min^{-1}), calculated using the data from the non-stationary regime during the light phase, are listed in Table 3 (further details on the fitting profiles are reported in Fig. S4). As can be noticed from C/C_0 profiles reported in Fig. 5, there is an abrupt slope variation for SLTNR15 after 40 min under UV irradiation. Less notably, the same behavior is observed in sample SLTNR20.

By analyzing photodegradation kinetics (Table S4), we assume that the sudden change in slope is influenced by the absorption phenomena occurring during the photolysis of MB. As a matter of fact, previous studies reported in literature, highlight pseudo-first and pseudo-second order kinetics associated with absorption phenomena, similar to what has been observed during our study [32]. Further investigations will be led to shed light on the actual mechanism and/or concurring processes.

The adsorption phenomenon of the MB taking place on the samples' surfaces during the dark interval equilibration time (30 min without light irradiation) can be also noticed from the C/C_0 plots.

The bare FTO glass substrate displays the highest capability of adsorbing MB molecules on its surface, significantly reducing its concentration up to 40 %. This can be ascribed to the fact that the pH of the MB solution is higher than the FTO point of zero charge (PZC) [33,34]. Instead, a correlation could be inferred between the decrease in the MB concentration (from 2 % to 17 %) and the increase in the O_2% in Ar. This means that the presence of less sub-stoichiometric TiO_{2-x}, having a higher number of surface exposed hydroxyl groups, leads to a higher number of interactions with MB's exposed functional groups. Under UV light, all photocatalysts show a very interesting catalytic performance, with a significant decrease in the MB concentration ranging from 30 % up to 99 %. As shown in Fig. 5c–f, both non-deposited SL and DL exhibit a certain degree of photocatalytic activity, revealing a behavior similar to all the other samples. The SLTNR15 is the most photoactive one, showing a kinetic constant for MB degradation around $9 \bullet 10^{-3}$ and a dye photodegradation ability of 99 % after 360 min. From XRD analysis and SEM images it can be stated that sample SLTNR15 possesses desired vertically aligned morphology and similar band gap energy value as sample DLTNR15 (having identical stoichiometry). However, from degradation profiles it is evident that SLTN15 exhibits strikingly different photocatalytic activity. This could stem from a combination between the rationally designed structure and the sub-stoichiometric sputtering deposition with 15% O_2 atmosphere, leading to an overall enhancement of the photocatalytic efficiency.

Careful comparison between single and double layer photodegradation profiles could open to the consideration that all SL samples performance is overall superior to DL. Since the goal of this work designing TiO_2/TiO_{2-x} nanostructures were to enhance photocatalytic efficiency under solar light irradiation, XTNRY were tested under the same operating conditions also using standard simulated solar light

Table 3
Degradation efficiency (% Dr) and k values for all the samples both under UV and Simulated Solar Light (SS) irradiation.

Sample	UV % Dr	SS % Dr	$k_{UV} \pm \delta_{kuv}$ (10^{-3} min^{-1})	$k_{ss} \pm \delta_{kss}$ (10^{-3} min^{-1})
SLTNR	36	73	-	-
DLTNR	43	78	-	-
SLTNR10	32	70	1.6 ± 0.2	4.9 ± 0.4
DLTNR10	53	65	8 ± 1	4.2 ± 0.6
SLTNR15	99	86	9 ± 1	6.8 ± 0.5
DLTNR15	44	70	2.8 ± 0.4	3.5 ± 0.5
SLTNR20	66	65	4.9 ± 0.5	6.3 ± 0.5
DLTNR20	53	70	2.4 ± 0.3	3.0 ± 0.4

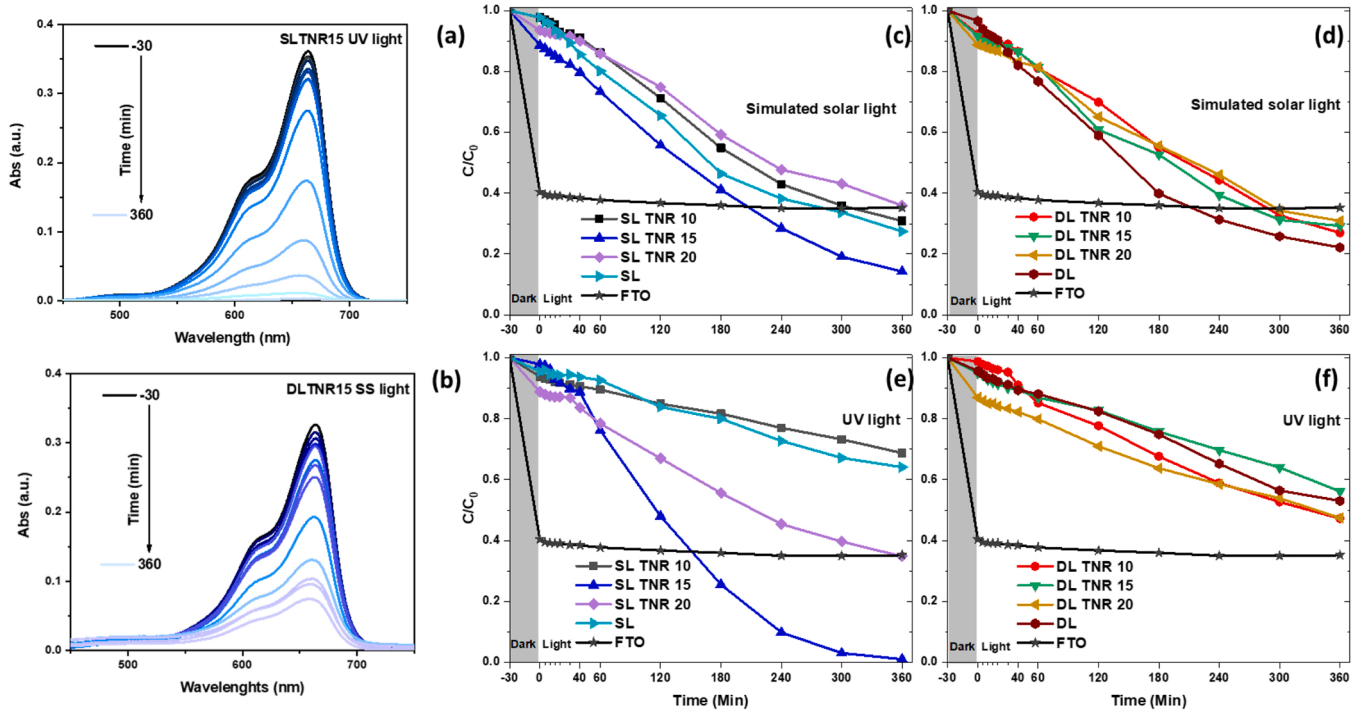

Fig. 5. Methylene blue (a,b) absorption spectra for SLTNR15 under UV and DLTNR15 under simulated solar (SS) light. Photodegradation curves of the investigated samples under (c, d) simulated solar light and (e, f) UV light irradiation at room temperature and atmospheric pressure.

irradiation. In general, every sample is showing an enhanced efficiency towards MB degradation under simulated solar light, with no exceptions (Table 3). The catalytic behavior of these systems is in accordance with their optical characterization: the band edge absorption redshift may be responsible for the overall increase in the photocatalytic efficiency. Even in this case, the best performing sample is SLTNR15, reaching a MB degradation of 86 % with a k value around $7 \bullet 10^{-3}$, thus confirming previous statements.

Since the recyclability of a catalyst is very important for its practical use, stability and reusability tests were carried out on sample SLTNR15 under UV light irradiation with the previous operating conditions. As shown in Fig. 6a, after three recycling processes, the SLTNR15 sample was not only still active towards MB dye degradation under UV light, suggesting a very good physico-chemical stability, but it also showed an improved photodegradation efficiency. This result could suggest a long-term application of the proposed catalyst in water treatment.

Since wastewaters sources can be found in a great range of pH, we exposed the synthesized catalyst to acidic and basic conditions and carried photodegradation process under UV light irradiation with the purpose of understanding the role of pH on the surface of the catalyst. Two different photocatalysis were carried at pH 4.0 and 9.0 both with sample SLTNR20 (Fig. 6b). Being MB a positively charged dye, its adsorption on the catalyst surface strongly depends on the charge of the catalyst surface itself. Point of zero charge values reported for TiO_2 are ranging from 5.0 and 6.2 [33–38], while the MB solution pH has been measured to be 6.2. TiO_2 surface is very sensitive to the presence of H^+ ions in the solution, since it is rich in terminal hydroxyl groups. Therefore, the surface catalyst is positively charged when the solution pH is below the PZC, conversely hydroxyl groups are deprotonated leaving the surface negatively charged when above the PZC. As it can be noticed from Fig. 6b, there are two opposite trends at pH 4.0 and 9.0, respectively. In acidic conditions, the positively charged surface of the catalyst attracts a higher number of oxidizing species. The latter can interact with positively charged MB molecules, which can be degraded almost by 100 after 360 min, without any adsorption phenomena onto the catalyst surface. On the contrary, in alkaline conditions the hydroxyl groups exposed on the catalyst surface are deprotonated. In this case, the adsorption phenomena easily occur, because of the electrostatic interactions. Hence, the strong decrease of the C/C_0 curve at pH 9.0 is not related to the photodegradation process.

Photodegradation processes under acidic and basic conditions were also carried out for the pristine FTO. The efficiency of SLTNR15 sample in both acidic and basic conditions compared with a bare FTO substrate was then investigated. Although FTO conductive layer promoted the formation of electron/hole pairs being active for the photodegradation of MB (Fig. S5), photolysis of MB under acid/alkaline conditions with SLTNR15 reached higher degradation efficiency (100 % degradation after 40 min and 98 % after 240 min under pH 4 and 9, respectively), thus proving the effectiveness of the TiO_2/ TiO_{2-x} system.

4. Conclusions

TiO_2 thin films are widely used in the field of heterogeneous photocatalysis to promote the degradation of organic pollutants in wastewater. To improve surface-to-volume ratio, ease adsorption/desorption mechanisms, avoid fast charge recombination processes and lower the wide TiO_2 band gap, a homojunction between two different oxygen rich/deficient TiO_2 layers has been proposed. According to SEM analyses, TiO_2 vertically aligned nanorods grown on the conductive side of a FTO glass were obtained through hydrothermal treatment in acidic conditions by optimizing the seeding process via spin coating. The average diameter was estimated to be of (78 ± 4) nm for SL and (68 ± 5) nm for DL, revealing that the number of seed layer deposition influenced the diameter growth generated by a large number of nucleation sites. By RF magnetron sputtering deposition, a homogeneous layer of thin TiO_{2-x} nanorods was then generated to form three different homojunctions by tuning the oxygen partial pressure in sputtering argon atmosphere at 10 %, 15 % and 20 %, respectively, inducing a substoichiometry in the structure that is reported by other authors to be consistent with oxygen vacancies. It should be mentioned that a distortion in the TiO_2 structure cannot be ruled out as a possibility, as suggested by XPS results. Both TiO_2 nanorods and TiO_{2-x} layer showed the same crystalline phase (rutile) as confirmed by XRD pattern. AFM studies confirmed what was previously observed by SEM. Rather uniform nanorod arrays were obtained, with nanostructures having an average lateral dimension of 80 nm (SLTNR sample) and of about 20 nm for the sputtered sample (SLTNR15). Moreover, AFM highlighted a decrease in the surface roughness due to the introduction of substoichiometric titania thin film, as expected. Photocatalytic activity has been investigated by monitoring the photodegradation of methylene blue (MB), chosen as target water contaminant, both under UV and simulated solar light irradiation at room temperature and atmospheric pressure. A MB degradation up to 99 % and 85 % under UV and simulated solar irradiation, respectively, was achieved for the best performing sample (SLTNR15) laying the groundwork for new environmental applications to enhance dye degradation industrial processes.

CRediT authorship contribution statement

Nicolò Spigariol: Conceptualization, Methodology, Formal analysis, Investigation, Data curation, Writing – original draft. **Letizia Liccardo:**

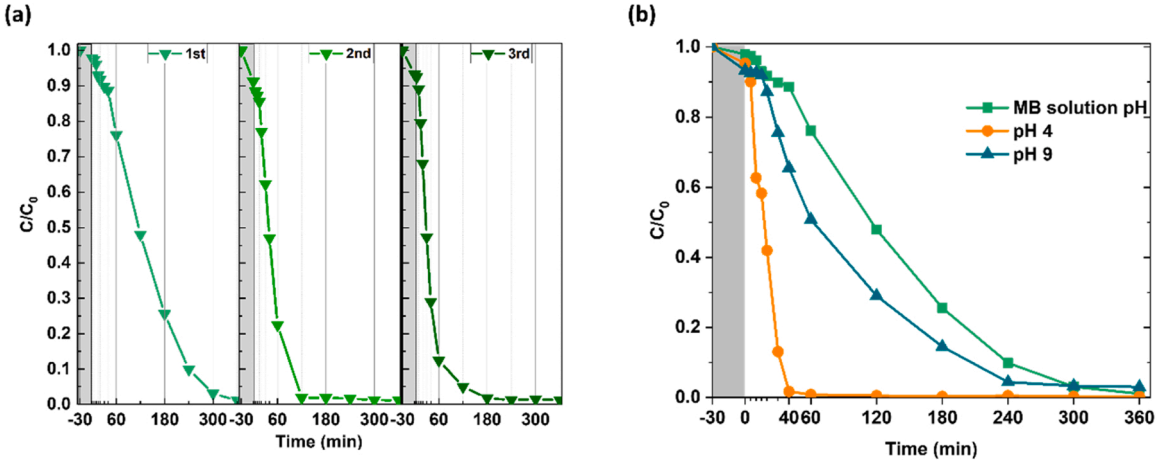

Fig. 6. (a) Reusability test for sample SLTNR15 performed under UV irradiation (b) Photocatalytic activity behavior in acidic and basic conditions.

Conceptualization, Methodology, Formal analysis, Investigation, Data curation, Writing – original draft, Writing – review & editing. **Edlind Lushaj:** Methodology, Formal analysis, Investigation, Data curation, Writing – review & editing. **Enrique Castellon:** Formal analysis, Methodology, Investigation, Resources, Data curation, Funding acquisition. **Isabel Barroso Martin:** Methodology, Formal analysis, Investigation, Data curation. **Federico Polo:** Investigation, Resources, Supervision, Funding acquisition, Writing – review & editing. **Alberto Vomiero:** Conceptualization, Resources, Supervision, Funding acquisition, Writing – review & editing. **Elti Cattaruzza:** Conceptualization, Investigation, Resources, Supervision, Funding acquisition, Writing – review & editing. **Elisa Moretti:** Conceptualization, Investigation, Resources, Supervision, Funding acquisition, Writing – review & editing.

Declaration of Competing Interest

The authors declare that they have no known competing financial interests or personal relationships that could have appeared to influence the work reported in this paper.

Data Availability

Data will be made available on request.

Acknowledgments

A.V. acknowledges financial support from the Kempe Foundation, the Knut och Alice Wallenberg Foundation (Grant no. KAW 2016.346), and the ÅFORSK Foundation. A.V. acknowledges Ca' Foscari University of Venice for SPIN2019 project. The authors acknowledge Mr. Tiziano Finotto from the Department of Molecular Sciences and Nanosystems, Ca' Foscari University of Venice, Italy, for his support on the XRD measurement. I.B.M. and E.R.C thank to Ministerio de Ciencia e Innovación of Spain, Grants PID2021-126235OB-C32 and TED2021-130756B-C31, and FEDER funds.

Appendix A. Supporting information

Supplementary data associated with this article can be found in the online version at doi:10.1016/j.cattod.2023.114134.

References

[1] T.O. Ajiboye, O.A. Oyewo, D.C. Onwudiwe, Simultaneous removal of organics and heavy metals from industrial wastewater: a review, Chemosphere 262 (2021), 128379, https://doi.org/10.1016/j.chemosphere.2020.128379.
[2] S. Anandan, V. Kumar Ponnusamy, M. Ashokkumar, A review on hybrid techniques for the degradation of organic pollutants in aqueous environment, Ultrason. Sonochem. 67 (2020), 105130, https://doi.org/10.1016/j.ultsonch.2020.105130.
[3] S. Varjani, P. Rakholiya, T. Shindhal, A.V. Shah, H.H. Ngo, Trends in dye industry effluent treatment and recovery of value-added products, J. Water Process Eng. 39 (2021), 101734, https://doi.org/10.1016/j.jwpe.2020.101734.
[4] C.R. Holkar, A.J. Jadhav, D.V. Pinjari, N.M. Mahamuni, A.B. Pandit, A critical review on textile wastewater treatments: possible approaches, J. Environ. Manag. 182 (2016) 351–366, https://doi.org/10.1016/j.jenvman.2016.07.090.
[5] C. Alberoni, I. Barroso-Martin, A. Infantes-Molina, E. Rodriguez-Castellon, A. Talon, H. Zhao, S. You, A. Vomiero, E. Moretti, Ceria doping boosts methylene blue photodegradation in titania nanostructures, Mater. Chem. Front. 5 (2021) 4138–4152, https://doi.org/10.1039/d1qm00068c.
[6] M. Telkhozhayeva, B. Hirsch, R. Konar, E. Teblum, R. Lavi, M. Weitman, B. Malik, E. Moretti, G.D. Nessim, 2D TiS_2 flakes for tetracycline hydrochloride photodegradation under solar light, Appl. Catal. B Environ. 318 (2022), 121872, https://doi.org/10.1016/j.apcatb.2022.121872.
[7] G. Ciamician, The photochemistry of the future, Science 36 (1912) 385–394, https://doi.org/10.1126/science.36.926.385.
[8] D. Ma, H. Yi, C. Lai, X. Liu, X. Huo, Z. An, L. Li, Y. Fu, B. Li, M. Zhang, L. Qin, S. Liu, L. Yang, Critical review of advanced oxidation processes in organic wastewater treatment, Chemosphere 275 (2021), 130104, https://doi.org/10.1016/j.chemosphere.2021.130104.
[9] P. Naliwajko, J. Strunk, Photocatalysis – the heterogeneous catalysis perspective, Heterog. Photocatal. (2021) 101–126, https://doi.org/10.1002/9783527815296.ch5.
[10] M.R. Al-Mamun, S. Kader, M.S. Islam, M.Z.H. Khan, Photocatalytic activity improvement and application of UV-TiO_2 photocatalysis in textile wastewater treatment: a review, J. Environ. Chem. Eng. 7 (2019), 103248, https://doi.org/10.1016/j.jece.2019.103248.
[11] M.T. Noman, M.A. Ashraf, A. Ali, Synthesis and applications of nano-TiO_2: a review, Environ. Sci. Pollut. Res. 26 (2019) 3262–3291, https://doi.org/10.1007/s11356-018-3884-z.
[12] E. Moretti, E. Cattaruzza, C. Flora, A. Talon, E. Casini, A. Vomiero, Photocatalytic performance of Cu-doped titania thin films under UV light irradiation, Appl. Surf. Sci. 553 (2021), 149535, https://doi.org/10.1016/j.apsusc.2021.149535.
[13] L. Liccardo, E. Lushaj, L. Dal Compare, E. Moretti, A. Vomiero, Nanoscale ZnO/α-Fe_2O_3 heterostructures: toward efficient and low-cost photoanodes for water splitting, Small Sci. 2 (2022) 2100104, https://doi.org/10.1002/smsc.202100104.
[14] J. Liu, L. Zhu, S. Xiang, H. Wang, H. Liu, W. Li, H. Chen, Cs-doped TiO_2 nanorod array enhances electron injection and transport in carbon-based $CsPbI_3$ perovskite solar cells, ACS Sustain. Chem. Eng. 7 (2019) 16927–16932, https://doi.org/10.1021/acssuschemeng.9b04772.
[15] Q. Guo, C. Zhou, Z. Ma, X. Yang, Fundamentals of TiO_2 photocatalysis: concepts, mechanisms, and challenges, Adv. Mater. 31 (2019) 1901997, https://doi.org/10.1002/adma.201901997.
[16] L. Pan, S. Wang, J. Xie, L. Wang, X. Zhang, J.J. Zou, Constructing TiO_2 p-n homojunction for photoelectrochemical and photocatalytic hydrogen generation, Nano Energy 28 (2016) 296–303, https://doi.org/10.1016/j.nanoen.2016.08.054.
[17] M. Iraj, F.D. Nayeri, E. Asl-Soleimani, K. Narimani, Controlled growth of vertically aligned TiO_2 nanorod arrays using the improved hydrothermal method and their application to dye-sensitized solar cells, J. Alloy. Compd. 659 (2016) 44–50, https://doi.org/10.1016/j.jallcom.2015.11.004.
[18] Z. Miao, G. Wang, L. Li, C. Wang, X. Zhang, Fabrication of black TiO_2/TiO_2 homojunction for enhanced photocatalytic degradation, J. Mater. Sci. 54 (2019) 14320–14329, https://doi.org/10.1007/s10853-019-03900-2.
[19] Z. Li, S. Wang, J. Wu, W. Zhou, Recent progress in defective TiO_2 photocatalysts for energy and environmental applications, Renew. Sustain. Energy Rev. 156 (2022), 111980, https://doi.org/10.1016/j.rser.2021.111980.
[20] X. Wang, L. Mayrhofer, M. Hoefer, S. Estrade, L. Lopez-Conesa, H. Zhou, Y. Lin, F. Peiró, Z. Fan, H. Shen, L. Schaefer, M. Moseler, G. Braeuer, A. Waag, Facile and efficient atomic hydrogenation enabled black TiO_2 with enhanced photoelectrochemical activity via a favorably low-energy-barrier pathway, Adv. Energy Mater. 9 (2019) 1900725, https://doi.org/10.1002/aenm.201900725.
[21] G. Greczynski, L. Hultman, *X-ray photoelectron spectroscopy*: towards reliable binding energy referencing, Prog. Mater. Sci. 107 (2020), 100591, https://doi.org/10.1016/j.pmatsci.2019.100591.
[22] G. Greczynski, L. Hultman, The same chemical state of carbon gives rise to two peaks in X-ray photoelectron spectroscopy, Sci. Rep. 11 (2021) 11195, https://doi.org/10.1038/s41598-021-90780-9.
[23] A. Houas, H. Lachheb, M. Ksibi, E. Elaloui, C. Guillard, J.M. Herrmann, Photocatalytic degradation pathway of methylene blue in water, Appl. Catal. B Environ. 31 (2001) 145–157, https://doi.org/10.1016/S0926-3373(00)00276-9.
[24] J. Shao, W. Sheng, M. Wang, S. Li, J. Chen, Y. Zhang, S. Cao, In situ synthesis of carbon-doped TiO_2 single-crystal nanorods with a remarkably photocatalytic efficiency, Appl. Catal. B Environ. 209 (2017) 311–319, https://doi.org/10.1016/j.apcatb.2017.03.008.
[25] S. Kaya, O. Ozturk, L. Arda, Roughness and bearing analysis of ZnO nanorods, Ceram. Int. 46 (2020) 15183–15196, https://doi.org/10.1016/j.ceramint.2020.03.055.
[26] J. Yang, J. Du, X. Li, Y. Liu, C. Jiang, W. Qi, K. Zhang, C. Gong, R. Li, M. Luo, H. Peng, Highly hydrophilic TiO_2 nanotubes network by alkaline hydrothermal method for photocatalysis degradation of methyl orange, Nanomaterials 9 (2019) 526, https://doi.org/10.3390/nano9040526.
[27] D. Rodríguez-Padrón, M. Algarra, L.A.C. Tarelho, J. Frade, A. Franco, G. De Miguel, J. Jiménez, E. Rodríguez-Castellón, R. Luque, Catalyzed microwave-assisted preparation of carbon quantum dots from lignocellulosic residues, ACS Sustain. Chem. Eng. 6 (2018) 7200–7205, https://doi.org/10.1021/acssuschemeng.7b03848.
[28] D. Polidoro, A. Perosa, E. Rodríguez-Castellón, P. Canton, L. Castoldi, D. Rodríguez-Padrón, M. Selva, Metal-free N-doped carbons for solvent-less CO_2 fixation reactions: a shrimp shell valorization opportunity, ACS Sustain. Chem. Eng. 10 (2022) 13835–13848, https://doi.org/10.1021/acssuschemeng.2c04443.
[29] E. Rodríguez-Aguado, A. Infantes-Molina, A. Talon, L. Storaro, L. León-Reina, E. Rodríguez-Castellón, E. Moretti, Au nanoparticles supported on nanorod-like TiO_2 as catalysts in the CO-PROX reaction under dark and light irradiation: effect of acidic and alkaline synthesis conditions, Int. J. Hydrog. Energy 44 (2019) 923–936, https://doi.org/10.1016/j.ijhydene.2018.11.050.
[30] P. Makuła, M. Pacia, W. Macyk, How to correctly determine the band gap energy of modified semiconductor photocatalysts based on UV-vis spectra, J. Phys. Chem. Lett. 9 (2018) 6814–6817, https://doi.org/10.1021/acs.jpclett.8b02892.
[31] M. Basu, A.K. Sinha, M. Pradhan, S. Sarkar, A. Pal, C. Mondal, T. Pal, Methylene blue-Cu_2O reaction made easy in acidic medium, J. Phys. Chem. C 116 (2012) 25741–25747, https://doi.org/10.1021/jp308095h.
[32] E.D. Revellame, D.L. Fortela, W. Sharp, R. Hernandez, M.E. Zappi, Adsorption kinetic modelling using pseudo-first order and pseudo-second order rate laws: a review, Clean. Eng. Technol. 1 (2020), 100032 https://doi.org/10.1016/j.clet.2020.100032.
[33] S. Haq, W. Rehman, M. Waseem, Adsorption efficiency of anatase TiO_2 nanoparticles against cadmium ions, J. Inorg. Organomet. Polym. Mater. 29 (2019) 651–658, https://doi.org/10.1007/s10904-018-1038-x.

[34] L. Tan, Z. Liu, C. Zhou, L. Ding, Combined factors influencing the surface charge and aggregation behaviors of TiO_2 nanoparticles in the presence of humic acid and UV irradiation, J. Nanopart. Res. 23 (2021) 191, https://doi.org/10.1007/s11051-021-05315-0.

[35] Q. Xiang, X. Ma, D. Zhang, H. Zhou, Y. Liao, H. Zhang, S. Xu, I. Levchenko, K. Bazaka, Interfacial modification of titanium dioxide to enhance photocatalytic efficiency towards H_2 production, J. Colloid Interface Sci. 556 (2019) 376–385, https://doi.org/10.1016/j.jcis.2019.08.033.

[36] M. Zeng, Influence of TiO_2 surface properties on water pollution treatment and photocatalytic activity, Bull. Korean Chem. Soc. 34 (2013) 953–956, https://doi.org/10.5012/bkcs.2013.34.3.953.

[37] C. Navas-Cárdenas, N. Benito, E.E. Wolf, F. Gracia, Tuning activity of $Pt/FeO_x/TiO_2$ catalysts synthesized through selective-electrostatic adsorption for hydrogen purification by prox reaction, Int. J. Hydrog. Energy 47 (2022) 20867–20880, https://doi.org/10.1016/J.IJHYDENE.2022.04.192.

[38] F. Azeez, E. Al-Hetlani, M. Arafa, Y. Abdelmonem, A.A. Nazeer, M.O. Amin, M. Madkour, The effect of surface charge on photocatalytic degradation of methylene blue dye using chargeable titania nanoparticles, Sci. Rep. 8 (2018) 7104, https://doi.org/10.1038/s41598-018-25673-5.